applied optics

Airborne four channel fiber coupled vector laser Doppler anemometer system

Oliver Kliebisch, Matthias Damm, and Peter Mahnke*

Institute of Technical Physics, German Aerospace Center (DLR), Pfaffenwaldring 38-40, Stuttgart, 70569, Germany
*peter.mahnke@dlr.de

Received 16 June 2023; revised 31 July 2023; accepted 5 August 2023; posted 7 August 2023; published 25 August 2023

Using an airborne vector laser Doppler anemometer (LDA) to measure the air flow outside of the boundary layer of an airplane is a promising optical technique. Measurement of the primary flight data like true airspeed, the angle of attack, and the angle of sideslip can be directly derived from the measured wind vector. We developed an experimental system with interchangeable telescopes to study the change in the LDA sensitivity and signal rate, depending on the focusing of the measurement beam. The system has a real-time-capable field programmable gate array data acquisition system, which also can record full data dumps for off-line analysis. This paper presents the first results of an airborne measurement campaign. The true airspeed is measured with an residual error of 1% compared to the five-hole flow sensor. The angle of sideslip and the angle of attack show a standard deviation of the residual error of 0.6° for the angle of sideslip and 0.2° for the angle of attack.

https://doi.org/10.1364/AO.498171

1. INTRODUCTION

Airborne laser Doppler anemometer (LDA) experiments like the ones realized in the European Union projects (NESLIE/DANIELA [1] and AIM2 [2]) have shown the success of single particle detection based systems as possible air data sensors. The publications of Spuler *et al.* [3,4] and Cooper *et al.* [5] demonstrated a single channel LDA based on volumetric scattering. An early scanning airborne single particle LDA based on a CO_2 laser was reported by Rahm [6].

An alternative approach to measure the wind vector is high resolution spectroscopy of Rayleigh scattering of the air demonstrated by Watkins *et al.* [7,8] called molecular optical air data system (MOADS). This so called "direct-detection" LDA requires bulky injection seeded pulsed single frequency UV lasers or high power cw UV lasers, which has not, to the best of our knowledge, been published so far, and sensitive interferometers. This approach has the clear advantage to be independent on the purely statistical existence of particles in the air, but has completely other issues regarding the technical implementation in an airplane. Another advantage and problem of this technique is the spectral broadening of the laser pulse by the scattering process. This enables gas temperature measurement but lowers the resolution of the Doppler shift measurement. Because of the high technical requirements, the direct detection technique is mostly used to detect clear air turbulence [9–11]. Another example of an airborne direct detection lidar is the ALADIN airborne demonstrator, a Doppler wind lidar [12].

The advantage of an LDA as an air data sensor is that it is inherently calibrated due to the ability to reconstruct the full wind vector [13] with respect to the airplane by measuring the air flow outside the boundary layer of the airplane. Conventional air data sensors, which measure the wind vector related air data, are pitot tubes [14] and angle of attack or angle of sideslip vanes. These sensors need a large amount of calibration, due to their mounting point within the boundary layer of the plane. Therefore, this technique is suited to calibrate conventional pitot tube sensors [5], angle of attack vanes and angle of sideslip indicators. If used in the particle detection regime, the sensor furthermore provides information about its operational status, data quality, and single particle measurement event frequency. A classical pitot tube or a five-hole probe can be influenced by humidity or dirt clogging the probe. Also, pitot tube covers might be left on these without detection. These systems usually cannot detect erroneous measurements, which could mean that the measured air data result might be wrong without notice. Even as a secondary sensor system, airplanes could benefit from an optical air data system that would offer enhanced safety by increasing the data reliability. The design of the LDA system discussed in this study shares similarities with the NESLIE/DANIELA [1] approach in terms of the optical layout and data processing [15]. Our goal was to enhance the system's effectiveness in various conditions and applications, serving as an optical air data sensor. The AIM2 project [2] leveraged LDA for in-flight calibration of existing sensors, focusing on an optimal arrangement of optical transceivers to achieve

high accuracy. However, there were instances of signal loss in certain situations.

Our design was guided by specific research objectives. First, we aimed to examine various real-time signal processing methods, while also capturing the direct photodiode raw signal. This would allow for the development of improved processing algorithms using actual flight data. Second, we intended to validate an end-to-end model [16] of the LDA system, particularly regarding the optimal selection of the optical parameters of the transceiver for a single particle scattering LDA.

In the subsequent sections, we will elaborate on the LDA system and our design choices, followed by initial results from an airborne measurement campaign.

2. EXPERIMENTAL SETUP

The design of our airborne four channel LDA was derived from our previous design, which we used to characterize the LDA [16]. A schematic of the setup is depicted in Fig. 1. It uses a 1550 nm double-sideband (DSB) fiber laser (Koheras BASIK, NKT Photonics) as the master oscillator for the master oscillator power amplifier architecture. The laser has two outputs: a monitor port with 1 mW output power, which serves as homodyne local oscillator reference channel and the main output with 10 mW that is sent through a fiber-coupled 80 MHz accouso-optic frequency shifter (AOF). The frequency-shifted first-order light can be used as a heterodyne local oscillator reference channel. The zero order of the AOF is split into two channels and amplified by two 2 W Er:doped fiber amplifiers (Koheras BOOSTIK, NKT Photonics). The two amplified channels are split into four 1 W fiber coupled output channels. Each amplifier output is guided through a fiber optic circulator (PMCIR-3-A-1550-900-5-0.8-FA-1W, Opneti) to an optical system transceiver, which images the fiber facet into the air. The backscattered signals are brought to interference with the local oscillator using a 50:50 fiber coupler (PNH1550R5A2, Thorlabs), and the signal is detected using a balanced avalanche photodiode (APD) receiver. The APD receiver was chosen due to the low available local oscillator power of 0.25 mW. The local oscillator reference channel can be chosen by a fiber optic switch.

Each photodiode signal is then digitized by a high-speed analog-to-digital converter (ADC) with 250 MS/s and 16-bit vertical resolution. The resolution was chosen to have a maximum dynamic range from shot noise to large signals. The angles of the transceivers were chosen in a way that the expected Doppler shift of the light within the flight envelope does not exceed the range of 5–120 MHz.

3. INTEGRATION OF THE LDA

The LDA system is integrated in a three-unit 19-inch rack box, which is shown in Fig. 2. The box is designed to withstand the acceleration forces necessary for air worthiness. It has a forced air cooling for the electronics and fiber laser systems. Furthermore, it serves as power distribution for the other systems present in the rack: a MicroTCA computer, keyboard and monitor drawer, and timeserver. The fiber interferometer with the balanced photodetectors inside the LDA system is shielded to prevent electromagnetic interference; i.e., from the acousto-optical frequency shifter. The system is fiber coupled to the transceivers using metal protected FC-APC coupled fibers.

4. FIBER INTERFEROMETER AND BALANCED DETECTORS

A fiber-coupled balanced APD detector was developed using fiber pigtailed 55 µm InGaAs APDs (KPDEA005L-SB11-FCAP-N, Kyosemi) with a bandwidth of 3 GHz, a capacitance of 0.5 pF, and a breakdown voltage of 45 V [17]. The transimpedance amplifier was designed using a two-stage approach. The amplifier schematic is depicted in Fig. 3. As the first stage a OPA847 amplifier was chosen with a 1 kΩ transimpedance gain [18,19]. The amplifier in this configuration will show a slight gain peaking. Therefore, a one-stage low-pass filter is used

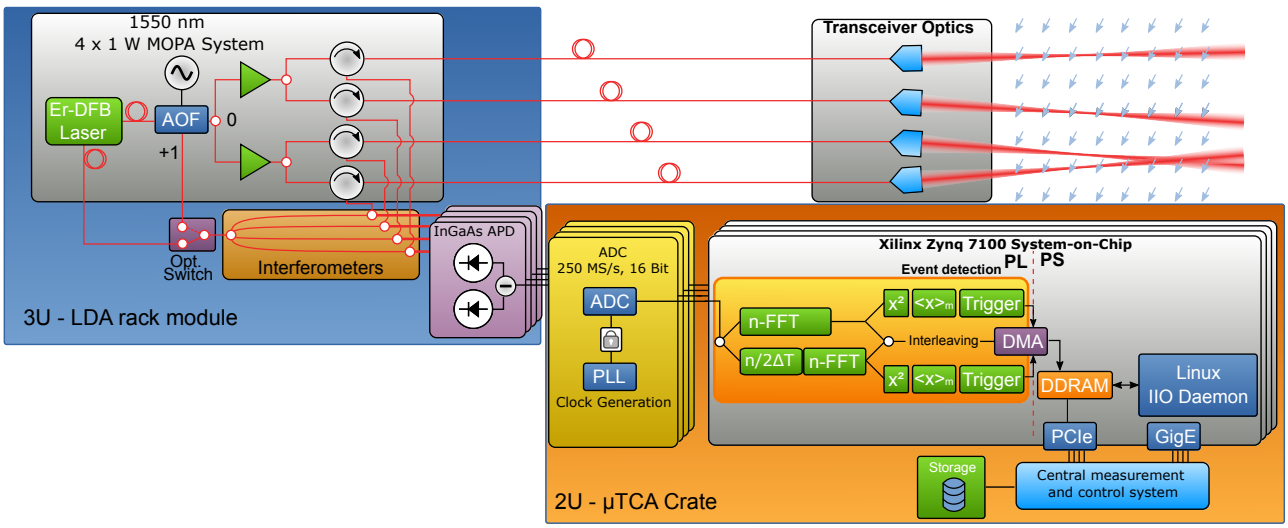

Fig. 1. Schematic of the four channel LDA setup. The system is divided into three parts: the LDA rack module, the µTCA data acquisition system, and the transceiver optics. The LDA rack module include the fiber laser and laser amplifier system, the circulators, and the fiber interferometers. Figure 5 shows a detailed sketch of the free space optical setup.

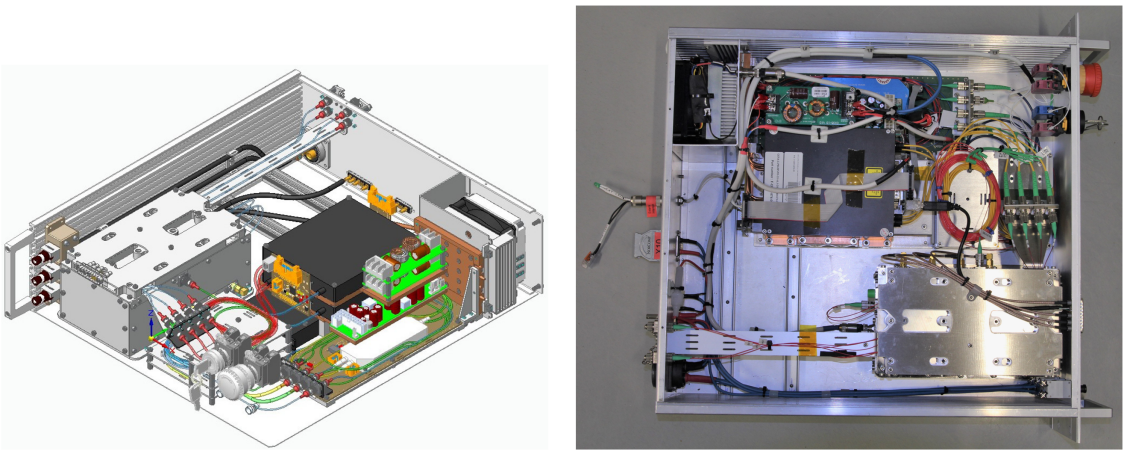

Fig. 2. CAD rendering and photo of the 19-inch LDA rack module. The fiber interferometer and balanced APD detectors are integrated in a nickel-plated box to ensure the electromagnetic compatibility of the sensor and suppress the external high-frequency signals.

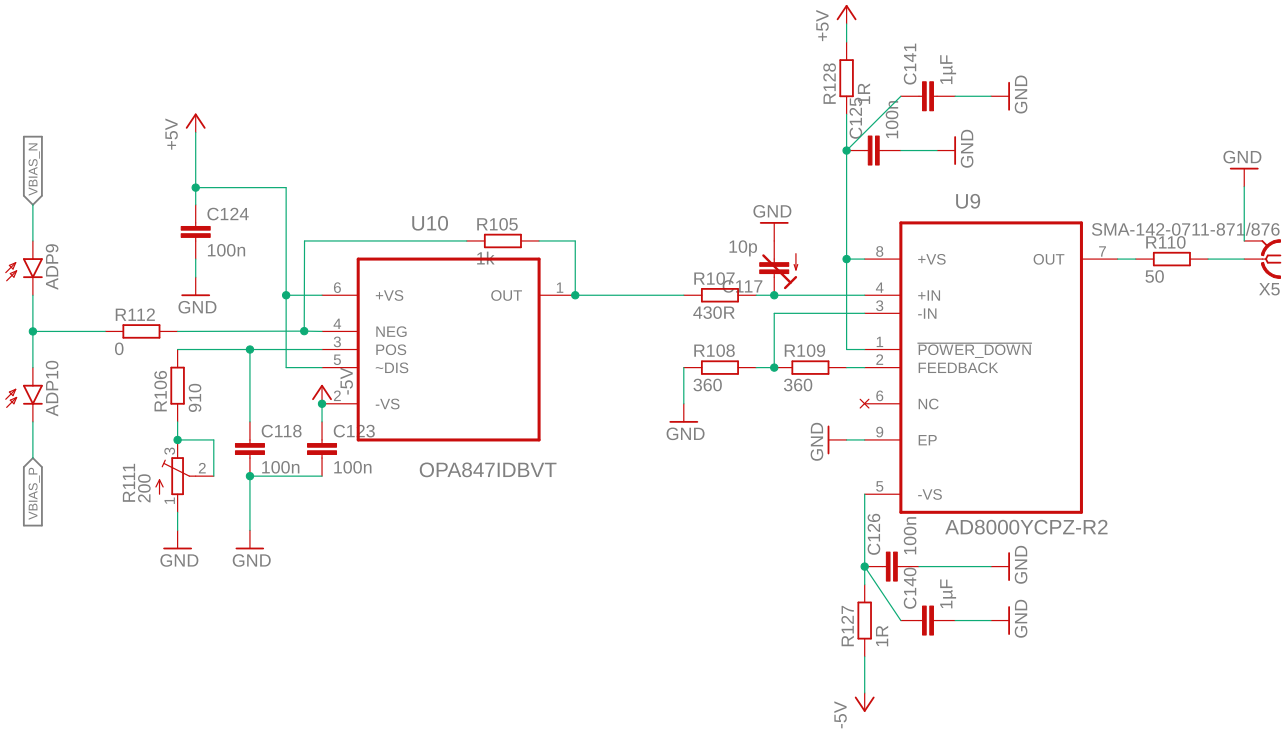

Fig. 3. Schematic of one channel of the balanced photodetector.

to flatten the gain in front of the second amplifier stage. The first stage amplifier must be designed close to the photodiodes without any copper layers in the layout to avoid stray capacitance, which will limit the bandwidth of this stage. The second stage amplifier is an AD8000 used as 50 Ω high slew rate line driver. The reverse offset bias voltages of the APDs could be adjusted using a 12-bit digital-to-analog converter amplified by a LTC6090 high-voltage operational amplifier by a factor of approximately 10. This enables computer control of the avalanche gain and balancing of the photodiodes. The output current of the bias amplifier was limited by a S-102T current-limiting diode in the output stage of the amplifier to protect the APDs from overcurrent. Supplement 1 has a detailed schematic.

The balanced detector is designed to have a bandwidth exceeding 200 MHz. For optimal performance, a well-filtered power supply was designed.

5. DATA ACQUISITION SYSTEM

A 19-inch, two-unit MicroTCA system was chosen as the data acquisition system. The MicroTCA standard includes thermal and power management. The MicroTCA.2 and MicroTCA.3 standards define the ruggedness and conduction cooling of the components. The system features a XEON-based control computer and four ZYNQ 7100 field programmable gate array (FPGA) cards. A 16-bit 250 MSamples ADC FPGA Mezzanine Card (FMC) is installed on each FPGA card for analog data

acquisition. An AD9467 from Analog Devices Inc. was used as the ADC. We designed an FMC-compatible ADC board that is electrically compatible to the design of the evaluation board AD9467-FMC-250EBZ of this chip. The FPGA serves multiple purposes in the system. It is used to transfer the data from the ADC to the memory and directly to the main computer. Furthermore, streamed interleaved fast Fourier transforms are used for real-time data processing algorithms on the FPGA [20]. Through this real-time signal processing, real-time spectral triggering is implemented [21]. The spectral triggering engine consists of two interleaved streamed 2048 samples fast Fourier transforms denoted as "n-FFT" in Fig. 1. The delay is denoted as "$\frac{n}{2}\Delta t$". To generate the trigger, the power spectrum of the spectral stream is calculated (x^2 in Fig. 1), optionally averaged ($\langle x \rangle_n$), and compared with spectrally masked trigger levels. If a signal event is detected, the raw spectral data is transferred to the main computer. The main computer evaluates the Doppler shifts of the triggered signal spectra by performing a center frequency estimation on the power spectral data. This frequency estimation is performed by a nonlinear least-squares fit of a Gaussian function to the measured LDA particle spectrum. The Doppler shift Δf_D, its uncertainty σ_{f_D}, and the signal strength s_{fd} are obtained and stored for each triggered event. The signal strength is related to the position where the particle passes the laser beam and the scattering cross section of the particle (size). The fast back-plane of the MicroTCA system and the fast solid-state drive also enable direct recording of four channels with 1000 MSa/s, which result in 2000 MByte/s data. This directly recorded data is useful to improve the real-time data processing. The direct recorded data can be used to optimize the real-time evaluation implemented on the FPGA board by performance comparison of the FPGA real-time algorithm with off-line evaluation of the recorded data. Time synchronization and position recording of the system is achieved by using a Meinberg Lantime M300 NTP GPS Timeserver.

The airplane is equipped with a Rosemount 585 noseboom five-hole sensor system. During the measurement flights, the aircraft systems also record this data, which is used for reference and comparison. Figure 4 shows the noseboom and the integration of the transceiver telescopes in the airplane.

A. Vector Reconstruction

After the aforementioned frequency estimation has been conducted for each individual channel of the LDA system, the relative wind vector can be reconstructed. First, the data is interpolated onto a regular time grid using either a zero- or first-order spline. This is necessary because each channel measures statistically independent single particle events that are not aerodynamically independent and happen with random temporal spacing. Another approach would be Kalman filtering or ROSE filtering of the data [15,22], which would result in an error estimate for the interpolated data. Furthermore, this allows the direct comparison of the data with noseboom measurements recorded with a 10 Hz data rate.

The Doppler shift for the i-th channel can be written as

$$\Delta f_{\mathrm{D},i} = -\frac{2}{\lambda}\boldsymbol{v}\cdot\boldsymbol{e}_i. \tag{1}$$

Here, $\boldsymbol{v}$ is the true relative wind vector, $\boldsymbol{e}_i$ is the unit vector of the laser beam direction (i.e., the normalized wavevector $\boldsymbol{e}_i = \boldsymbol{k}_i/|k_i|$), and λ is the laser wavelength. It is beneficial to express the unit vector using the azimuth and elevation angle in spherical coordinates. The set of Doppler shifts from all n channels ($n = 4$ for our system) can be written as a vector $\boldsymbol{\Delta} f_{\mathrm{D}} = (\Delta f_{\mathrm{D},1}, \ldots, \Delta f_{\mathrm{D},n})^T$. Likewise, the concatenation of the unit vectors forms the $n \times 3$ matrix $\boldsymbol{K} = (\boldsymbol{e}_i, \ldots, \boldsymbol{e}_n)^T$. The measurement of n LDA channels can be thus written as

$$\boldsymbol{\Delta} f_{\mathrm{D}} = -\frac{2}{\lambda}\boldsymbol{K}\boldsymbol{v}. \tag{2}$$

For $n > 3$, this is an over-constrained problem and can be treated as a linear regression. Therefore, we use the Moore–Penrose inverse of $\boldsymbol{K}$, which is given as $\boldsymbol{K}^+ = (\boldsymbol{K}^T\boldsymbol{K})^{-1}\boldsymbol{K}^T$ and solve Eq. (2) for $\boldsymbol{v}$ to get the reconstructed velocity vector $\boldsymbol{v}_r$ as

$$\boldsymbol{v}_r = -\frac{\lambda}{2}\boldsymbol{K}^+\boldsymbol{\Delta} f_{\mathrm{D}}. \tag{3}$$

We extend the regression to the feasible generalized least squares method by using the standard error σ_i of the i-th frequency estimate of the Doppler shift to define the weight matrix

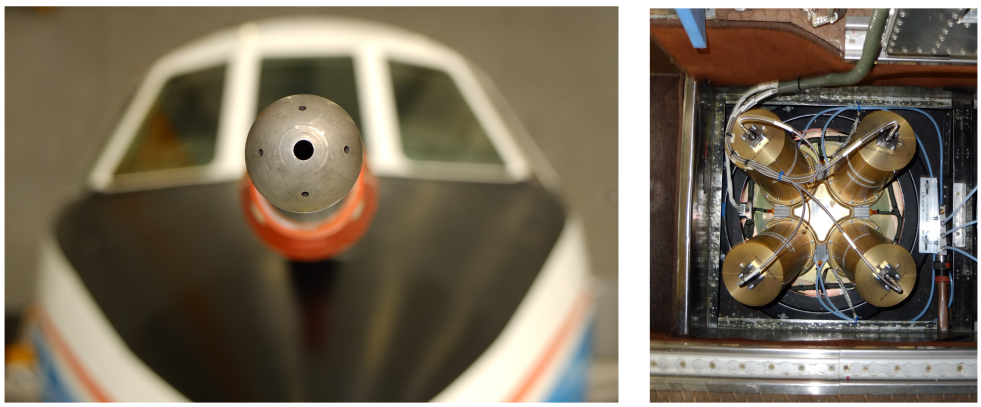

Fig. 4. Left: Rosemount 585 five-hole flow sensor of the DLR Falcon 20-E5 experimental aircraft. Right: Integration of the LDA transceivers in the airplane floor.

$$\boldsymbol{W} = \begin{bmatrix} \sigma_1^{-1} & & 0 \\ & \ddots & \\ 0 & & \sigma_n^{-1} \end{bmatrix}. \tag{4}$$

The reconstructed velocity is then given by

$$\hat{\boldsymbol{v}}_r = -\frac{\lambda}{2}\left(\boldsymbol{K}^T \boldsymbol{W} \boldsymbol{K}\right)^{-1} \boldsymbol{K}^T \boldsymbol{W} \boldsymbol{\Delta} f_{\mathrm{D}}. \tag{5}$$

The true air speed (TAS), the angle of attack (AoA), and the angle of sideslip (AoS) can be calculated from the reconstructed velocity vector by

$$\mathrm{TAS} = |\hat{\boldsymbol{v}}_r|, \tag{6}$$

$$\mathrm{AoS} = \arctan2(\hat{\boldsymbol{v}}_{r,x}, \hat{\boldsymbol{v}}_{r,y}), \tag{7}$$

$$\mathrm{AoA} = \arccos\left(\frac{\hat{\boldsymbol{v}}_{r,z}}{\mathrm{TAS}}\right) - \frac{\pi}{2}. \tag{8}$$

If there is at least one degree of freedom $\zeta = n - 1 \geq 1$ (i.e., $n >= 4$) the uncertainty of the regression can be calculated using the residual

$$r = \boldsymbol{\Delta} f_{\mathrm{D}} + \frac{2}{\lambda} \cdot \boldsymbol{K} \hat{\boldsymbol{v}}_r. \tag{9}$$

The parameter χ_ζ^2 is used to assess the fidelity of the fit and

$$\chi_\zeta^2 = \frac{\boldsymbol{r}^T \boldsymbol{W} \boldsymbol{r}}{\zeta}. \tag{10}$$

This allows us to calculate the variance-covariance matrix

$$\boldsymbol{M}_\beta = \chi_\zeta^2 \cdot \left(\boldsymbol{K}^T \boldsymbol{W} \boldsymbol{K}\right)^{-1}. \tag{11}$$

The uncertainty is then given by

$$\delta \hat{\boldsymbol{v}}_r = \sqrt{\mathrm{diag}(\boldsymbol{M}_\beta)}, \tag{12}$$

and the corresponding uncertainties of the TAS, AoA, and AoS can be calculated using Gaussian error propagation.

B. Aerodynamic Correction/Calibration

Because the mounting of the transceivers still has a rotational degree of freedom, corrections to the vectors must be applied. The mounting errors are corrected using simple rotational matrices. A rotational correction in the plane of the flange is performed until cross-talk between the angle of sideslip and angle of attack is minimized. Following these rotations in the axis of the plane and in the axis of the wings will adjust the origin of the angle of sideslip and the angle of attack Furthermore, we observed aerodynamic errors due to the system's mounting position far from the airplane's nose. The measured airspeed showed only small deviations. The airflow around the fuselage of the airplane at the LDA position reduces the angle of attack and increases the angle of sideslip. The linear corrections

$$\mathrm{TAS} = 1.02\mathrm{TAS}_{\mathrm{Raw}},$$

$$\mathrm{AoA} = 1.5\mathrm{AoA}_{\mathrm{Raw}},$$

$$\mathrm{AoS} = 0.7\mathrm{AoS}_{\mathrm{Raw}}.$$

were chosen to make the measured angles comparable to the noseboom data. These corrections are only affected marginally when changing the optical configuration.

6. OPTICAL TRANSCEIVER PORT

In the floor section of the Dassault Falcon 20 research aircraft dedicated viewports allow the installation of two photo windows with a 49 cm [23] open aperture. The bottom window openings are protected by a shutter door during takeoff and landing. For the LDA system, a special flange was constructed with four 100 mm diameter 15 mm thick quartz windows. The windows were anti-reflection coated with an environmentally stable ion beam sputtered coating for 1550 nm (Laseroptik GmbH). The windows are mounted under a 15° angle with respect to the floor of the airplane. The 15° angle was chosen to ensure the airplane's velocity range of 40–240 m/s and the angular range of ±5° that the Doppler shift is in the range of 10–110 MHz [see Eq. (1)]. Four different transceiver telescopes can be mounted onto this flange. The telescopes are interchangeable to study the effect of different optical configurations on the signal. We implemented telescopes with multiple measurement distances, focusing the beam 50 cm, 1 m, and 25 m away from the airplane hull. The flange is shown in Fig. 5.

The telescopes have been designed to have different Rayleigh lengths and focal distances. They maintain the beam quality of

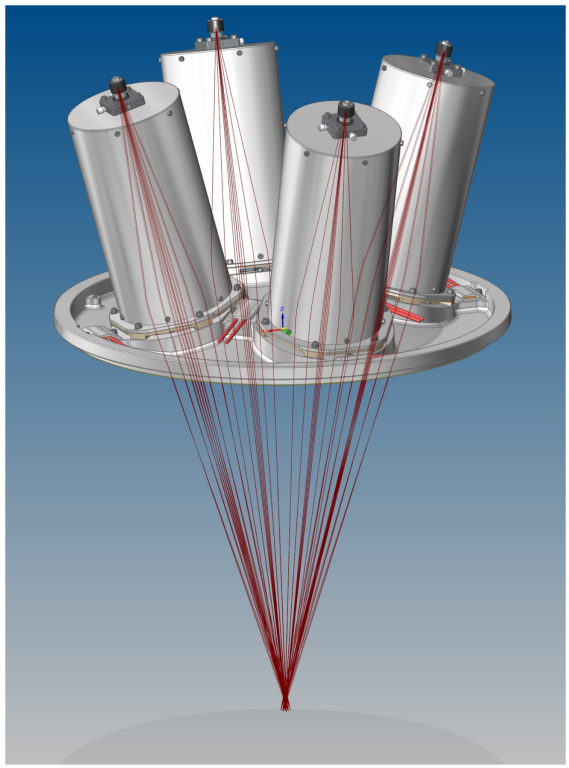

Fig. 5. CAD rendering of the flange of the four channel transceiver telescopes. The flange is mounted in the floor section of the airplane and has a diameter of approximately 50 cm. Each depicted telescope has an open aperture of 9 cm. The beam propagation is sketched in red lines for a fiber end imaging distance of 500 mm. Bistatic operation is avoided; the observation volumes are only close to each other and do not overlap.

Table 1. Available Transceiver Telescopes

Telescope	Imaging Ratio	Open Aperture	Object and Image Distance
200 mm Schaeffter and Kirchhoff fiber collimator with a 500 mm focusing lens	1:2.5	50 mm	200 mm, 500 mm
Custom aspherical telescope	1:2	90 mm	250 mm, 500 mm
Custom aspherical telescope	1:4	90 mm	250 mm, 1 m

the single-mode fiber (PM1550-HP, 10.5 µm mode field diameter, Thorlabs). Four telescopes were built, and the properties are listed in Table 1. The focal spot size qualitatively influences the signal in the following manner: a smaller spot size results in a shorter Rayleigh length and a higher peak intensity. Smaller particles can be detected and the spectral width is broadened due to the smaller passing time (shorter pulses). These factors and the particle statistics influence the optimal parameters for the evaluation algorithms (like. e.g., the Fourier transform length). Currently, we work with a fixed Fourier transform length. The FPGA, however, would allow the implementation of variable length Fourier transforms or multiple different-length processing engines.

7. FIRST RESULTS

Several flight tests with various telescope configurations were conducted from Oberpfaffenhofen Airport in April 2022 and Braunschweig-Wolfsburg Airport in October 2022. A typical test flight included various flight situations, which enable the evaluation of our measurement system. To vary the angle of attack, the flight speed was varied in a constant height. For sideslip angle variation, a steady-heading sideslip maneuver was intentionally executed. The natural concentration of aerosol shows a strong variance, depending on the atmospheric boundary layer and clouds.

In Fig. 6 the signal strength and spectral trigger event frequency from a flight day is shown. A mixed configuration of two 500 mm imaging distance 1:2 aspheric telescopes and two 1000 mm imaging distance 1:4 telescopes was used in this flight. A channel-resolved plot of the signal statistics can be found in Supplement 1. The upper-left plot shows the particle event frequency in a single LDA channel. The lower-left plot shows the probability density function (PDF) of the fitted signal strength scaled on the trigger threshold in time intervals of a minute. In the lower-right plot, the average PDF for the flight is plotted as a blue line and the minute resolution PDFs are plotted as dots. The dot size was chosen to represent the event frequency. It is noteworthy that the variation of signal strength was nearly independent from the trigger event frequency. The signal strength was dependent on the aerosol type present in the air. The particles, which can be detected by the LDA were estimated to be bigger than 0.1 µm; in [16], we showed the detection of low albedo 1 µm particles. For a 400 times higher reflectivity a 10 times smaller particle should be detectable. These particles are mainly accumulation mode aerosols, which are log-normal distributed aerosols with a maximum in the range of 0.1–1 µm [24]. Within the atmospheric boundary layer and dependent on the weather, some large particles (e.g., pollen, Saharan dust, marine aerosols, and black carbon) also can be observed. Note that the signal strength distribution for this flight does not depend on the signal trigger rate; therefore, it can be concluded

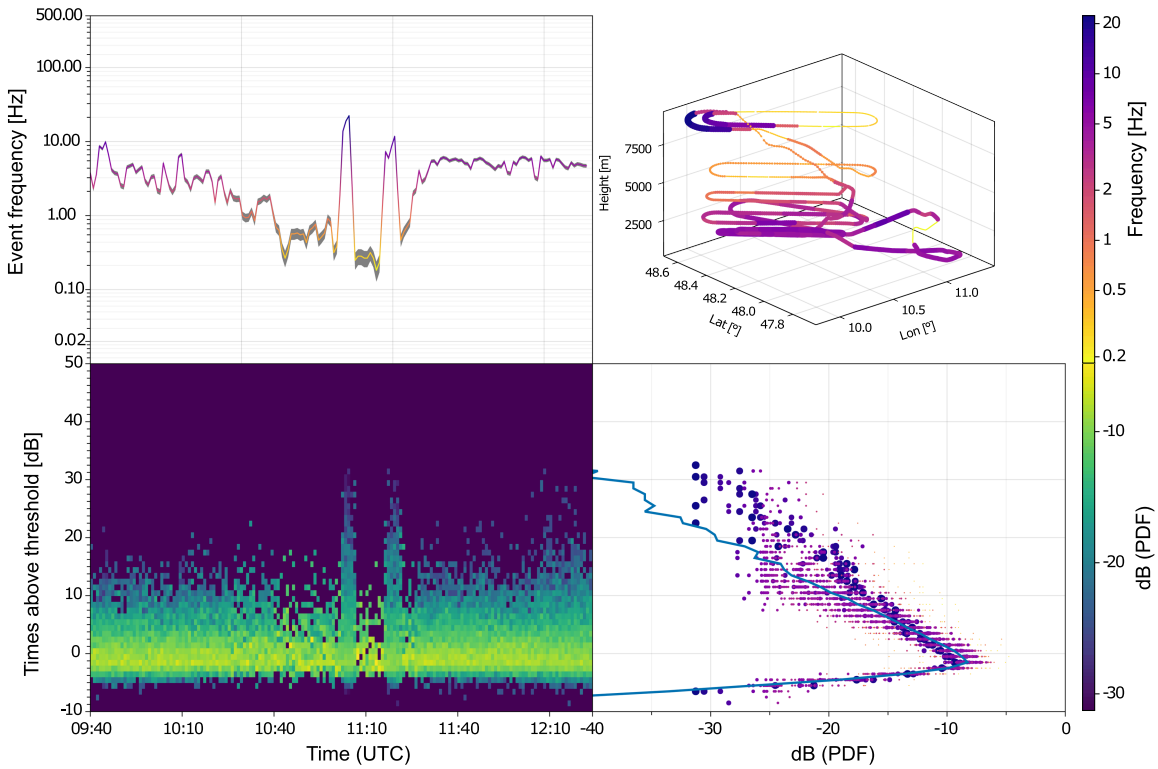

Fig. 6. Signal strength distribution and spectral trigger event frequency of the test flight on 11 April 2022.

that the particle size distribution in our observation showed only small variations. The signal strength distribution can be described as a convolution of the instrument function [16] and the distribution of the effective scattering cross section of the particles. The trigger frequency, however, is quite dependent on the aerosol content of the air mass that the airplane passes by. In our measurement, we flew race track patterns in different heights. Within the boundary layer, 9:40–10:30 UTC and 11:30–12:20 UTC, we observed approximately 5–10 spectral trigger events per second. At our peak altitude, we passed either cirrus clouds or contrails, twice resulting in a high trigger rate and particles with higher scattering cross section (11:00–11:05 UTC and 11:15–11:20 UTC). The upper-right plot illustrates the trigger event frequency on the flight path in a 3D projection plot. The trigger event frequency is color-coded onto the flight path, and the passing of the cirrus clouds can be observed in the upper-left part of the plot.

The comparison of the LDA-derived TAS, AoA, and AoS with the noseboom measurements is depicted in Fig. 7. The measurements show a quite good correlation between the two systems, besides some mounting-position-dependent effects observed in certain flight maneuvers. For the true air speed, a standard deviation of the residual error of 1.8 m/s compared to the noseboom was observed. The standard deviation of the residual of the angle of attack was 0.2°. For the residual error of the angle of sideslip, a standard deviation of 0.6° was observed.

8. DISCUSSION

The system described here can be improved in several ways. Changing the APD balanced detector to PIN-diode balanced detectors would result in better temperature stability of the system's background noise. Sensitivity (the power spectral SNR, as shown in Fig 2. of [16]) of a shot-noise-limited PIN-diode detector is approximately five times better than the sensitivity of a shot-noise-limited APD detector. To operate the PIN-diode detector in the shot-noise-limited regime, a reference power of 5–10 mW is needed for a single channel. This higher reference power can be achieved by a one percent fiber coupler behind the EDFA stage. Further integration and better performance of the balanced detector by using dedicated photodiode transimpedance amplifiers with a differential analog signal driver stage would result in a more robust design because most high-speed ADCs have differential analog input stages. Therefore, the balun transformers needed for single-ended signal input could be omitted and the noise immunity could be improved by using differential signaling.

Higher laser output power, comparable to the 5 W system presented by Spuler *et al.* [4], would increase the sensitivity (power spectral SNR) by a factor of 5, but would limit the use of interconnected fiber optics. The interchangeable optics of the system are currently unique, but the angles of the optics could be optimized for best inversion of the wind vector.

In the design process and for service we decided not to splice the connections between the components. Each connection introduces some losses and reduces the polarization contrast in the system. These fiber connection related losses could be reduced by splicing the system.

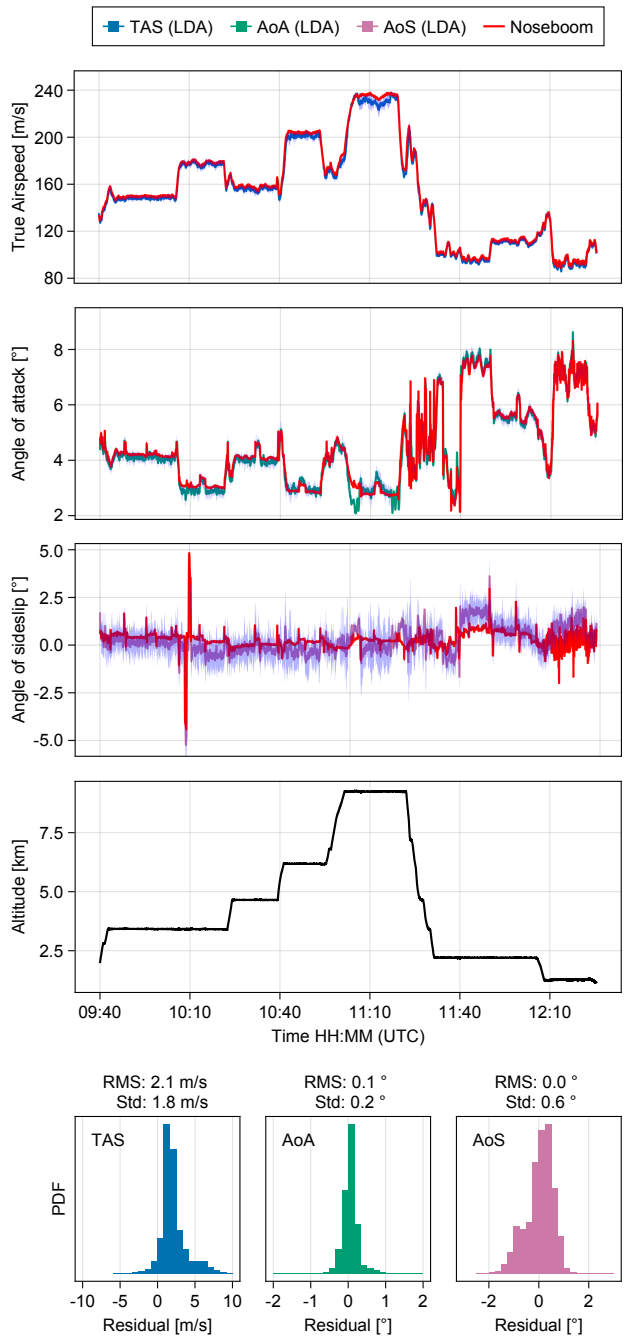

Fig. 7. Processed TaS, AoA, and AoS from the test flight on 11 April 2022. Noseboom data is depicted in red, and LDA data is shown with its error bars. The error bars are drawn in lighter colors. The deviation statistics between the noseboom data and LDA data are calculated for the whole flight.

The spectral trigger engine is also an algorithm that can be optimized to meet the variable signal pulse length due to the flight speed range from approximately 150 km/h to 870 km/h. An optimization aspect would be matching the length of the Fourier transform to the length of the scattering impulses. However, multiple trigger engines with different Fourier transform length would be needed. Performance evaluation using recorded data and synthetic data would be possible.

9. CONCLUSION

Our airborne experimental LDA system, which enabled us to directly record laser Doppler particle scattering data, proved in a measurement campaign to measure the wind vector with low deviations compared to a five-hole sonde. The system, however, can still be improved as discussed above. The presented system is suitable as a secondary air data sensor and reference system as proposed by Cooper *et al.* [5] and reported by Jentink *et al.* [1]. The recorded raw data and processed data are valuable to evaluate the design constraints of an optical air data sensor system.

Acknowledgment. The authors would like to thank S. Siegert for proofreading.

Disclosures. The authors declare no conflicts of interest.

Data availability. Data underlying the results presented in this paper are not publicly available at this time but may be obtained from the authors upon reasonable request.

Supplemental document. See Supplement 1 for supporting content.

REFERENCES

1. H. W. Jentink, H. Kannemans, and M. J. Verbeek, "In-flight evaluation of an optical standby air data system," Technical report NLR-TP-2010-436 (2010).
2. B. Augere, B. Besson, D. Fleury, D. Goular, C. Planchat, and M. Valla, "1.5 μm lidar anemometer for true air speed, angle of sideslip, and angle of attack measurements on-board Piaggio P180 aircraft," Meas. Sci. Technol. **27**, 054002 (2016).
3. S. M. Spuler, D. Richter, M. P. Spowart, and K. Rieken, "Optical fiber-based laser remote sensor for airborne measurement of wind velocity and turbulence," Appl. Opt. **50**, 842–851 (2011).
4. S. Spuler, M. Spowart, and D. Richter, "Development and application of an optical fiber-based laser remote sensor for airborne measurement of wind velocity," in *26th International Laser Radar Conference (ILRC)* (2012), pp. 1–4.
5. W. Cooper, S. Spuler, M. Spowart, D. Lenschow, and R. Friesen, "Calibrating airborne measurements of airspeed, pressure and temperature using a Doppler laser air-motion sensor," Atmos. Meas. Tech. **7**, 3215–3231 (2014).
6. S. Rahm, "Precursor experiment for an active true airspeed sensor," Opt. Lett. **26**, 319–321 (2001).
7. C. B. Watkins, C. J. Richey, P. Tchoryk, Jr., G. A. Ritter, P. B. Hays, C. A. Nardell, T. C. Willis, and R. Urzi, "Molecular optical air data system (MOADS) flight experiment," Proc. SPIE **5086**, 236–245 (2003).
8. C. B. Watkins, C. J. Richey, P. Tchoryk, Jr., G. A. Ritter, M. T. Dehring, P. B. Hays, C. A. Nardell, and R. Urzi, "Molecular optical air data system (MOADS) prototype II," Proc. SPIE **5412**, 10–20 (2004).
9. N. P. Schmitt, W. Rehm, T. Pistner, P. Zeller, H. Diehl, and P. Navé, "The AWIATOR airborne lidar turbulence sensor," Aerosp. Sci. Technol. **11**, 546–552 (2007).
10. G. J. Rabadan, N. P. Schmitt, T. Pistner, and W. Rehm, "Airborne lidar for automatic feedforward control of turbulent in-flight phenomena," J. Aircr. **47**, 392–403 (2010).
11. J. Herbst and P. Vrancken, "Design of a monolithic michelson interferometer for fringe imaging in a near-field, UV, direct-detection Doppler wind lidar," Appl. Opt. **55**, 6910–6929 (2016).
12. Y. Durand, E. Chinal, M. Endemann, R. Meynart, O. Reitebuch, and R. Treichel, "ALADIN airborne demonstrator: a Doppler wind lidar to prepare ESA's ADM-Aeolus explorer mission," Proc. SPIE **6296**, 62961D (2006).
13. Y. Yeh and H. Z. Cummins, "Localized fluid flow measurements with an He–Ne laser spectrometer," Appl. Phys. Lett. **4**, 176–178 (1964).
14. R. M. Muñoz, H. W. Mocker, and L. Koehler, "Airborne laser Doppler velocimeter," Appl. Opt. **13**, 2890–2898 (1974).
15. T. Katsibas, T. Semertzidis, X. Lacondemine, and G. Nikos, "Signal processing for a laser based air data system in commercial aircrafts," in *European Signal Processing Conference* (2008).
16. P. Mahnke, O. Kliebisch, and M. Damm, "Precise characterization of a fiber-coupled laser Doppler anemometer with well-defined single scatterers," Appl. Phys. B **125**, 1–10 (2019).
17. Kyosemi, "KP-A InGaAs avalanche photodiodes," KPDEA005-56F.
18. X. Ramus, "Transimpedance considerations for high-speed amplifiers," Texas Instruments Application Report SBOA122 (2009) https://www.ti.com/lit/an/sboa122/sboa122.pdf.
19. T. Instruments, "OPA847, wideband, ultra-low noise, voltage-feedback operational amplifier with shutdown," Texas Instruments Datasheet SBOS251E (2008), https://www.ti.com/lit/ds/symlink/opa847.pdf.
20. G. Bi and E. Jones, "A pipelined FFT processor for word-sequential data," IEEE Trans. Acoust. Speech Signal Process. **37**, 1982–1985 (1989).
21. O. Kliebisch and P. Mahnke, "Real-time laser Doppler anemometry for optical air data applications in low aerosol environments," Rev. Sci. Instrum. **91**, 095106 (2020).
22. R. Marchthaler, "Adaptive extended Kalman filter (ROSE-filter) for positioning system," arXiv, arXiv:2108.11321 (2021).
23. German Aerospace Research Establishment (DLR), "DLR Forschungsflugzeug FALCON E D-CMET," https://www.dlr.de/fb/PortalData/51/Resources/dokumente/kabinenlayout_falcon.pdf.
24. A. Petzold and B. Kärcher, *Aerosols in the Atmosphere* (Springer, 2012), pp. 37–53.